




Nonvolatile magnetization switching in a single-layer magnetic topological insulator

Huimin Sun ^{1,2,3,6}, Yizhou Liu^{4,6}, Daiqiang Huang^{1,2}, Yu Fu^{1,2,3}, Yu Huang^{1,2,3}, Mengyun He^{1,2,3}, Xuming Luo⁴, Wenjie Song⁵, Yang Liu^{1,2}, Guoqiang Yu ⁴ & Qing Lin He ^{1,2,3}✉

Magnetization in a ferromagnetic layer could be manipulated by the spin-orbit torque whose generation commonly relies on the spin-orbit coupling from the adjacent heavy-metal layer within the bilayer. The fact that the magnetic topological insulator possesses both the ferromagnetic order with perpendicular anisotropy and inherent spin-orbit coupling inspires to realize such a torque-induced magnetization switching without forming any heterostructure with other materials. Here, only using a single layer of magnetically-doped topological insulator $\text{Cr}:(\text{Bi,Sb})_2\text{Te}_3$, we realize a magnetization switching only by applying a large dc current. Assisted by the magnetic history, such a switching behaves nonvolatile under zero field but becomes volatile otherwise, as consistently shown by magnetoelectric transports and magneto-optical Kerr effect measurements. Static and quasistatic current are found to be equivalent for the switching. We propose that this switching may associate with the torque resulted from the spin-orbit coupling and the compositional asymmetry in the Cr-profile of the single layer.

¹International Center for Quantum Materials, School of Physics, Peking University, 100871 Beijing, China. ²Collaborative Innovation Center of Quantum Matter, 100871 Beijing, China. ³Interdisciplinary Institute of Light-Element Quantum Materials and Research Center for Light-Element Advanced Materials, Peking University, 100871 Beijing, China. ⁴Beijing National Laboratory for Condensed Matter Physics, Institute of Physics, Chinese Academy of Sciences, 100190 Beijing, China. ⁵Songshan Lake Materials Laboratory, Dongguan 523808 Guangdong, China. ⁶These authors contributed equally: Huimin Sun, Yizhou Liu. ✉email: qlhe@pku.edu.cn

Spin-orbit torques (SOTs) and SOT-driven magnetization switchings in ferromagnet/heavy-metal bilayers have been extensively explored owing to the potential applications in energy-efficient and ultrafast spintronic devices¹. Most of these SOT-devices employ the spin Hall effect^{2–4} and/or interfacial inverse spin-galvanic effect^{5–7}, which are believed to originate in the spin-orbit coupling from the heavy-metals and the hetero-interfaces. However, such SOTs are not exclusively inherited from the bilayers whereas, after the discoveries of the inverse spin Hall effect^{8–11} and charge-to-spin conversion^{12–19} in a single-layer ferromagnet without the nominal spin-orbit source from the heavy-metal, it has recently been revealed that the SOT can also be generated within the ferromagnet solely, which even allows to switch the magnetization of the ferromagnet itself^{20–25}. Although the mechanism of such SOTs remains elusive, its generation, detection, and exploitation have drawn significant attention, which enable the electrical control of the magnetization without any external polarizer and offer promising advantages in improving the device scalability and stability.

So far, this SOT has been observed in FeMn²⁶, Li₀-FePt^{20,21,27}, CoTb^{22,28,29}, Py^{30–32}, CoPt^{33–36}, Gd-Fe-Co³⁷, Mn₃Sn²⁴, FeTb²⁵, and Co₂MnGa²³, all of which are metallic and exhibit a dominant damping-like (DL) SOT over the field-like (FL) SOT in most cases. Among them, the role played by the spin-orbit coupling is found to be nonnegligible, whereas some of them possess spin Hall angles even comparable to those in heavy-metals. It is known that topological insulators (TIs) can serve as a powerful reservoir of spin-orbit coupling that the spin-momentum locking of surface electrons can be utilized for high-efficient spin accumulation and SOT-exertion. Therefore, TIs have been widely used to replace the heavy-metal in the bilayer to couple with the ferromagnet, via which the magnetization switchings with higher efficiencies and lower threshold current densities have been achieved^{38–45}. By incorporating with a small amount of magnetic dopants, the TI becomes ferromagnetic while the strong spin-orbit coupling can still be preserved, as exemplified by the archetypal material Cr-doped (Bi,Sb)₂Te₃.

Here, in a thin single-layer magnetic TI Cr-doped (Bi,Sb)₂Te₃, we discover a large DL-SOT accompanied with considerable unidirectional magnetoresistance (UMR) and nonlinear Hall effect. After demagnetizing the magnetic TI to zero field, the magnetization of the magnetic TI itself could be switched by applying a dc current solely. Based on the magnetoelectric transport and magneto-optical Kerr effect (MOKE) measurements, we found that such a switching, which was assisted by the magnetic history, behaved nonvolatile at zero field but otherwise volatile, which could be accomplished by either static or quasistatic current. We proposed that the SOT in the single-layer Cr-doped (Bi,Sb)₂Te₃ that probably originates in the compositional asymmetry of the Cr-profile may play a role in the observed switchings.

Results

Second harmonic measurements. To probe SOT in the single-layer magnetic TI, second harmonic magnetoresistance ($R_{\parallel}^{2\omega}$) and Hall resistance ($R_{\perp}^{2\omega}$) were tracked when rotating the applied magnetic field \mathbf{H} in the xy -, zx -, and zy -planes, as schematically shown in Fig. 1a, respectively. This is performed at 4.5 K by feeding an ac current $I_{ac} = 10 \mu\text{A}$ into the Hall bar along the x -direction and measuring the voltages with lock-in technique. As $R_{\parallel}^{2\omega}$ of the zx -scan only stems from the anisotropic magnetoresistance R_{AMR} perturbed by DL-SOT and magnetothermal effect (MTE) via⁴⁶:

$$R_{\parallel}^{2\omega} = -\frac{\Delta R_{AMR}}{2} \frac{h_{DL}}{H_K \cos\theta + H \cos(\theta_H - \theta)} \sin(2\theta) + C_{MTE} \sin(2\theta) \nabla T_z \quad (1)$$

where h_{DL} is the current-induced effective DL-field, H_K is the

effective anisotropy field, C_{MTE} is the coefficient for MTE, and ∇T_z represents the temperature gradient along the z -direction induced by Joule heating, the extraction of h_{DL} can be obtained by fitting $R_{\parallel}^{2\omega}$ data obtained above the saturation field of $\mu_0 H \geq 0.8\text{T}$ using Eq. (1). Here, $\Delta R_{AMR} = 3400 \Omega$ is obtained from the first harmonic magnetoresistance (R_{\parallel}^{ω}) when rotating $\mu_0 H = 3\text{T}$ in the xy -plane (Fig. 2b) and $H_K = 0.48\text{T}$ from the first harmonic Hall resistance when rotating various $\mu_0 H$ in the zx -plane, R_{\perp}^{ω} (Supplementary Note 1 and Supplementary Fig. 1). The first term of Eq. (1), which is related to the DL-SOT, has a magnetic field dependence of $H \cos(\theta_H - \theta)$, whereas the second term, which is related to MTE, is independent of the external magnetic field. Therefore, by fitting $R_{\parallel}^{2\omega}$ data under 1–3T (Fig. 1b and Supplementary Fig. 2), these two terms can be separated and h_{DL} is determined to be 0.65 mT. The corresponding SOT-efficiency $\xi_{SOT} = \frac{2eM_s h_{DL}}{h j_c}$ is about 12.4 as evaluated using parameters of the saturation magnetization $M_s = 35 \text{ kA/m}$ (Supplementary Fig. 3), the film thickness $t = 6 \text{ nm}$, and the current density $j_c = 3.33 \times 10^7 \text{ A/m}^2$. Such a ξ_{SOT} is much higher than those in metallic ferromagnet/heavy-metal bilayers^{47–49} and comparable to those in TI/ferromagnet bilayers^{43,44}. It is noted that the magnitude of $R_{\parallel}^{2\omega}$ is not very sensitive to the $\mu_0 H$ -strength, so there should be a large contribution from MTE, whose magnitude is almost independent with $\mu_0 H$.

Likewise, the UMR can be evaluated from $R_{\parallel}^{2\omega}$ when rotating in the xy - and zy -planes. $R_{\parallel}^{2\omega}$ in the xy -plane can be expressed as⁴⁶:

$$R_{\parallel}^{2\omega} = -\frac{\Delta R_{AMR}}{4} \frac{h_{FL}}{H} (\sin 3\varphi + \sin \varphi) + (C_{ANE} + C_{SSE}) \sin \varphi \nabla T_z + N_{ONE} H \sin \varphi \nabla T_z + R_{\parallel UMR} \sin \varphi \quad (2)$$

where h_{FL} is the current-induced effective FL-field, C_{ANE} and C_{SSE} are the coefficients for the anomalous Nernst effect (ANE) and spin Seebeck effect (SSE), N_{ONE} is the coefficient for the ordinary Nernst effect (ONE), and $R_{\parallel UMR}$ is the UMR, respectively. Experimentally, these terms could be distinguished from each other by their distinct angle- and H -dependences: h_{FL} contributes a $\sin 3\varphi$ component, ANE/SSE and their coefficients (C_{ANE} and C_{SSE}) are essentially H -independent, whereas ONE is H -linear; in TI-related systems, $R_{\parallel UMR}$ usually arises from the asymmetric magnon scattering due to the spin-momentum locking which results in a H^{-p} dependence with p close to 1^{50–52}. As the helicity of spin-momentum locking is opposite at the top and bottom surfaces, the corresponding scattering also has opposite sign. The UMR will be canceled out if the top and bottom surfaces are perfectly symmetric, but this ideal situation can never be achieved in any real sample. Hence, the presence of UMR suggests the structural asymmetry in the as-grown single-layer magnetic TI, which provides hints for the presence of SOT. Take the $R_{\parallel}^{2\omega}$ data under 3T in Fig. 1b as an example, it well follows a $\sin\varphi$ -behavior whereas the $\sin 3\varphi$ component is vanishingly small and, hence, the contribution from h_{FL} is negligible. Similar fittings are carried out in other $R_{\parallel}^{2\omega}$ data under various $\mu_0 H$, which are scatter-plotted in Fig. 1d. By fitting to these $\mu_0 H$ -dependent $\sin\varphi$ component, the H -independent, H -linear, and H^{-p} -dependent terms could be determined as 42.53, -3.52 , and -10.90Ω , respectively. This suggests that the H -independent ANE/SSE and H^{-p} -dependent UMR dominate $R_{\parallel}^{2\omega}$, while the H -linear ONE only takes a minor role. The above evaluation is cross-checked using $R_{\parallel}^{2\omega}$. Rotating

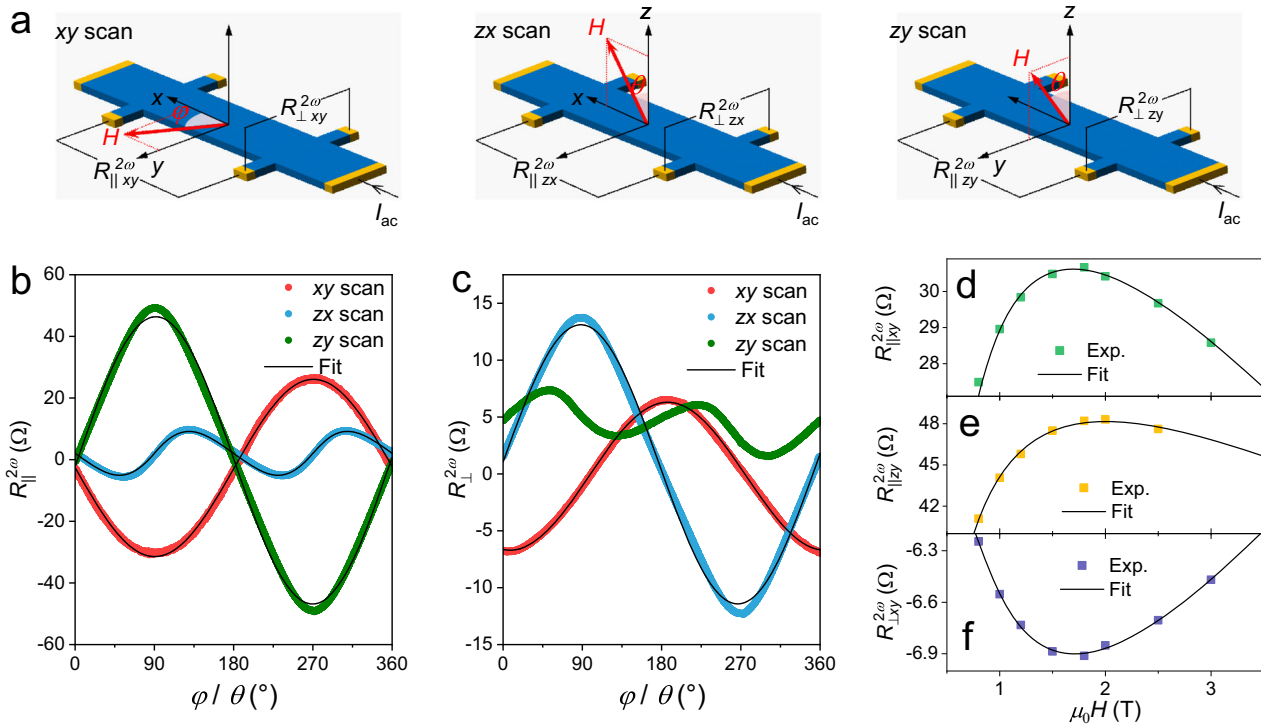


Fig. 1 The damping-like spin-orbit torque, unidirectional magnetoresistance, and nonlinear Hall effect. **a** Geometry of the measurements. The Hall bar is made of a single-layer magnetic topological insulator. **b, c** Second harmonic magnetoresistance ($R_{\parallel}^{2\omega}$) and Hall resistance ($R_{\perp}^{2\omega}$) recorded when rotating the magnetic field of 3T at 4.5 K in three different planes with fits. **d-f** Extracted field-dependent $R_{\parallel}^{2\omega}$ and $R_{\perp}^{2\omega}$ in different planes with fits.

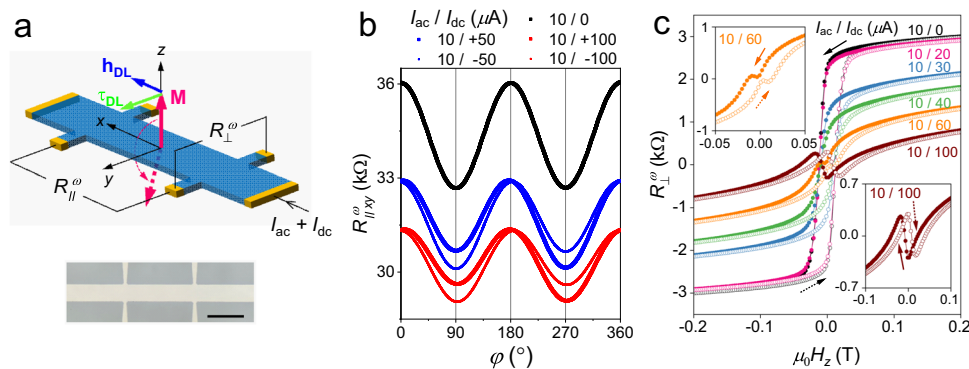


Fig. 2 Effects of the dc current. **a** Switchings of the out-of-plane magnetizations by the dc current under zero magnetic field. The geometry of the first harmonic magnetoresistance (R_{\parallel}^{ω}) and first harmonic Hall resistance (R_{\perp}^{ω}) measurements is also shown in the upper panel. (DL damping-like, \mathbf{M} magnetization, $\boldsymbol{\tau}_{\text{DL}}$ DL torque, \mathbf{h}_{DL} DL effective field.) The lower panel shows the optical image of the device. Scale bar: 100 μm . **b** R_{\parallel}^{ω} measured by applying different current combinations when rotating in the xy -plane. **c** $\mu_0 H_z$ -dependent R_{\perp}^{ω} measured by applying different current combinations as plotted by different colors. Insets are enlarged views.

in this plane, only the ANE, ONE, and UMR contribute via:

$$R_{\parallel zy}^{2\omega} = C_{\text{ANE}} \sin \theta \nabla T_z + N_{\text{ONE}} H \sin \theta \nabla T_z + R_{\parallel \text{UMR}} \sin \theta. \quad (3)$$

The extracted $\mu_0 H$ -dependent $R_{\parallel zy}^{2\omega}$ is scatter-plotted in Fig. 1e, the fitting to which evaluates the H -independent, H -linear, and H^2 -dependent contributions as 64, -3.95 , and -14Ω , respectively. These values essentially agree with those from $R_{\parallel xy}^{2\omega}$ except the H -independent term owing to the extra contribution from SSE in $R_{\parallel xy}^{2\omega}$ and/or a slight change of ANE after thermal cycling the sample. Therefore, UMR can be identified after excluding the thermal effects and SOT. To quantify UMR using the ratio of the second to first harmonic magnetoresistance over the applied ac current density j_{ac} , $\alpha = \left(\frac{R_{\parallel xy}^{2\omega}}{R_{\parallel xy}^{\omega}} \right) / j_{\text{ac}}$, we then acquire the

φ -dependent $R_{\parallel xy}^{\omega}$ under 3T in Fig. 2b, which follows the $\cos(2\varphi)$ relation with a periodicity of π . We could then determine $\alpha = 6.51 \times 10^{-6} \text{ cm}^2/\text{A}$, which is several orders of magnitude higher than those in metallic bilayers^{53,54} and comparable to those in TI-multilayers⁵². To obtain the direct signature of UMR, dc currents of opposite polarities $\pm I_{\text{dc}}$ are respectively added onto I_{ac} while the first harmonic voltages are measured using lock-in technique (Fig. 2b). In this way, a pronounced antisymmetric $R_{\parallel xy}^{\omega}$ between $\varphi = 90^\circ$ and 270° arises that $R_{\parallel xy}^{\omega}$ is higher (lower) when I_{dc} is parallel (antiparallel) to the y -axis. Such an antisymmetry is regarded as the signature of the unidirectional and bilinear magnetoresistance, showing that the reversal of $\mu_0 H$ is equivalent to the reversal of I_{dc} ^{55,56}. As shown in Supplementary Note 2, since $R_{\parallel xy}^{2\omega}$ inevitably comes with $R_{\parallel xy}^{\omega}$ in lock-in

measurements, ONE in $R_{\parallel xy}^{2\omega}$ will also contribute to the resulted $R_{\parallel xy}^{\omega}$, which hence complicates the estimation of UMR from $R_{\parallel xy}^{\omega}$. Anyway, such $R_{\parallel xy}^{\omega}$ also supports the existence of UMR in the single-layer magnetic TI as those extracted from $R_{\parallel xy}^{2\omega}$, and provides another method beyond the second harmonic method to probe the UMR, which is particularly useful for cases with negligible thermal effect or small $R_{\parallel xy}^{2\omega}$ signal.

The above evaluations are cross-checked by the second harmonic Hall resistance $R_{\perp}^{2\omega}$ of the xy -plane, which can be expressed by⁴⁶:

$$R_{\perp xy}^{2\omega} = \frac{\Delta R_{AMR}}{4} \frac{w}{l} \frac{h_{FL}}{H} (\cos 3\varphi - \cos \varphi) + \frac{R_{AHE}}{2} \frac{h_{DL}}{-H_K + H} \cos \varphi - C_{ANE} \frac{w}{l} \cos \varphi \nabla T_z - N_{ONE} H \frac{w}{l} \cos \varphi \nabla T_z + R_{\perp UMR} \cos \varphi \quad (4)$$

where $w = 50 \mu\text{m}$ and $l = 200 \mu\text{m}$ are the width and length of the Hall bar respectively, R_{AHE} is the resistance from the anomalous Hall effect (AHE), and $R_{\perp UMR}$ is the nonlinear Hall component of UMR. Note that the FL-SOT term should be excluded according to the analysis on $R_{\parallel xy}^{2\omega}$. Therefore, $R_{\perp xy}^{2\omega}$ should only follow a $\cos\varphi$ -periodicity, which is captured by the φ -dependent $R_{\perp}^{2\omega}$ data with the cosinusoidal fit in Fig. 1c. Similar to $R_{\parallel xy}^{2\omega}$ and $R_{\parallel zy}^{2\omega}$, since the remaining terms have different H -dependences, it is possible to separate them by fitting to the $\mu_0 H$ -dependent $R_{\perp xy}^{2\omega}$. Here, in addition to the H -independent, H -linear, and H^{-1} -dependences discussed above, the $(-H_K + H)^{-1}$ dependence that corresponds to the contribution from DL-SOT needs to be extracted separately. From the fit shown in Fig. 1f these terms are determined as -9.7 , 0.8 , 2.7 , and -0.17Ω , respectively. As expected from Eqs. (3) and (4), thermal terms of ANE and ONE in $R_{\perp xy}^{2\omega}$ and $R_{\perp zy}^{2\omega}$ should differ by $-w/l = -0.25$. After counting $-w/l$, the former two terms (i.e. ANE and ONE terms) become 38.8 and -3.2Ω , respectively. Compared with those extracted from $R_{\parallel zy}^{2\omega}$, i.e., 64 and -3.95Ω , the ONE term can reach a quantitative consensus, whereas a large contrast exists between these ANE terms. Besides the measurement uncertainty and angular misalignment in experiments, such a contrast probably comes from a H -linear UMR, which has been observed in the intrinsic TIs^{57,58}. Ideally, the $R_{\perp xy}^{2\omega}$ -measurement allows to quantify the DL-SOT but it may not be well compatible with a system with a perpendicular anisotropy (like the magnetic TI of this study) since a strong $\mu_0 H$ is required in this case. However, such a strong $\mu_0 H$ diminishes the contribution from DL-SOT and hence may cause larger measurement uncertainties due to the reduced magnetic susceptibility.

Magnetization switching by dc current. By applying I_{dc} to the single-layer magnetic TI, we detected a signature of magnetization switching particularly near zero magnetic field. As illustrated in Fig. 2a that the initial magnetizations are prepared to the out-of-plane and $\mu_0 H$ returns to zero. As a sizable DL-SOT is observed in the single layer, when I_{dc} is applied along the x -axis, the DL-SOT $\tau_{DL} = \mathbf{M} \times (\mathbf{M} \times \mathbf{y})$ will force the magnetization \mathbf{M} to switch to align with the DL effective field $\mathbf{h}_{DL} = h_{DL} \mathbf{M} \times \mathbf{y}$ and realize a magnetization switching. Generally, this scheme requires an in-plane $\mu_0 H$ parallel to the applied current for a deterministic switching, and the result is shown in Supplementary Fig. 4. When applying different magnetic fields along the x -direction ($\pm \mu_0 H_x$) in the setup of Fig. 1 and sweeping I_{dc} to drive the switching of R_{\perp}^{ω} , along with the change of the I_{dc} -polarity, R_{\perp}^{ω} switches sign for each $\pm \mu_0 H_x$. This test suggests that the SOT is successfully

induced in our single-layer magnetic TI. Surprisingly, under an out-of-plane field $\mu_0 H_z$ in Fig. 2c, when the role of I_{dc} is gradually promoted by increasing the relative magnitude of I_{dc} over I_{ac} (I_{ac} is always fixed at $10 \mu\text{A}$), the first harmonic Hall resistance R_{\perp}^{ω} at the saturation exhibits a successive decrease. When I_{dc} reaches $60 \mu\text{A}$, a pair of small zero-Hall plateaus appear near the coercivity (left inset in Fig. 2c); above this value, the hysteresis loop even switches sign as evidenced by the reversed loop direction (right inset in Fig. 2c). Regarding the origin of the observed switching, we try to exclude the Joule heating from the possible main mechanism as follows. As shown in Supplementary Note 3 and Supplementary Fig. 5, while a dc-dominant mixed current $I_{ac} + I_{dc} = 10 \mu\text{A} + 100 \mu\text{A}$ realized the switching at 4.5K , the ac current $I_{ac} = 110 \mu\text{A}$ with the similar heating-power to the former only heats up the sample without showing any trace of switching. This heating effect is supported by the fact that R_{\perp}^{ω} measured by applying such I_{ac} at 4.5K coincides with that by a much smaller $I_{ac} = 10 \mu\text{A}$ at an elevated sample temperature, i.e. 8K . The above results underline that the switching is caused by I_{dc} whereas I_{ac} only heats up the sample (otherwise the result using $I_{ac} = 110 \mu\text{A}$ should have shown the switching). That is, the directionality of the applied current is the key for switching, while the consequent Joule heating cannot induce or explain the nonvolatile switching.

As discussed above, the resulted R_{\perp}^{ω} may include some $R_{\perp}^{2\omega}$ component like thermal effects more than the AHE. This leads to a question whether the observed switching in R_{\perp}^{ω} really comes from the magnetization switching. To address this, the switching process in transport measurement is performed using pulse currents (I_p) in order to minimize the Joule heating and also reexamined using MOKE simultaneously as follows.

Switching by quasistatic current. The switching using I_p is found to be equivalent with that using static current, further diminishing the role played by Joule heating. The experiment is performed as follows: fully magnetizing the magnetic TI under $\mu_0 H_z = \pm 0.5 \text{T}$, i.e. $\pm M_z$, followed by sweeping to a specific magnetic field $\mu_0 H_z^*$; then injecting one or multiple I_p of various amplitudes and 200-ms length to the Hall bar. During this process, $I_{ac} = 1 \mu\text{A}$ constantly flows through the device so that R_{\perp}^{ω} can be always recorded by lock-in amplifier. In Fig. 3a, the gray loops are the full hysteresis loops measured using I_{ac} which serve as references. The Hall bar is fully magnetized under $\mp 0.5 \text{T}$ (left/right panel) before being demagnetized to zero field (i.e., $\mu_0 H_z^* = 0$) and fed by one $I_p = 50 \mu\text{A}$. Suddenly R_{\perp}^{ω} jumps from $\mp M_z$ to $\pm M_z$ during the application of I_p , signifying the magnetization switching under zero field. After this switching, I_p is removed but I_{ac} still sustains to track R_{\perp}^{ω} which gradually converges onto the full hysteresis loop when sweeping toward $\pm 0.5 \text{T}$. Results using $I_p = 20 \mu\text{A}$ and $100 \mu\text{A}$ are shown in Supplementary Fig. 6 which show similar behaviors. The magnitude of the sudden jump is found to increase when ramping I_p to $50 \mu\text{A}$, and saturate if ramping further. This signature is analogous to the SOT-induced magnetization switching in magnetic TI heterostructures^{39,40}, in which only a portion of magnetization can be switched no matter the current is further increased. To examine the equivalence of static and pulse current in switchings, various $\mu_0 H_z^*$ demagnetizing from $+0.5 \text{T}$ are adopted and $I_p = 200 \mu\text{A}$ is used (Supplementary Fig. 7) to sketch the $\mu_0 H_z$ -dependent R_{\perp}^{ω} switching loop, which is then used to compare with those obtained using $\pm I_{dc}$. These three curves are plotted in Fig. 3b, which show consistency after minimizing the Joule heating by I_p . This again proves that the switching mechanism associates with the directionality of the applied current, which excludes the Joule heating from the dominant

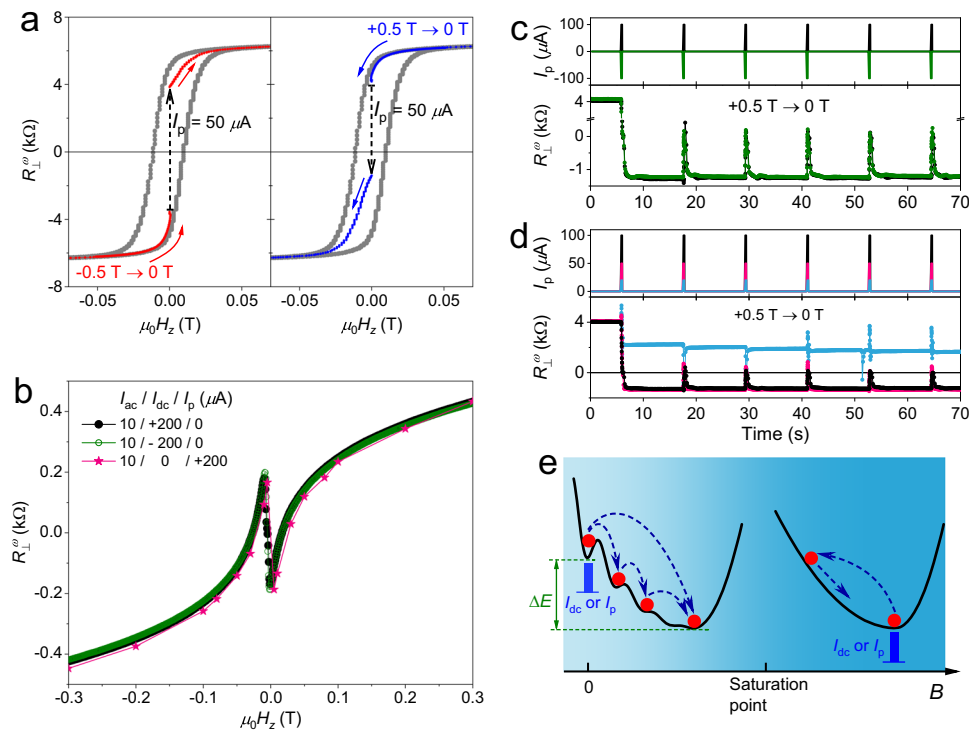


Fig. 3 Zero-field magnetization switchings probed by transports. **a** The first harmonic Hall resistance (R_{\perp}^{ω}) measured by I_{ac} (10 μ A) except a pulse current I_p (50 μ A, 200 ms) is applied under zero field, which results in a sudden jump in R_{\perp}^{ω} (dashed arrow). The gray loops are the full hysteresis loops measured using I_{ac} as references. **b** $\mu_0 H_z$ -dependent R_{\perp}^{ω} probed by different current configurations. **c, d** R_{\perp}^{ω} recorded when repeatedly applying I_p of different amplitudes under zero field. **e** Phenomenological explanation to the observed magnetization switching. The red circles represent the magnetic state, blue dashed lines indicate the possible transitions, and ΔE is the energy difference between different magnetic states. Activation energies given by various I_{dc} or I_p can drive the magnetic state out from different local minima to others (navy dashed arrows).

mechanism. Moreover, from the coincidence of the curves by $\pm I_{dc}$, one can find that both polarities function in the same way and the switching is polarity-independent. To further confirm this, multiple I_p of opposite polarities ($I_p = \pm 100 \mu$ A) are successively injected. As shown in Fig. 3c, after demagnetizing from +0.5T to 0, both I_p can quickly reduce R_{\perp}^{ω} from 4 to $-1.2 \text{ k}\Omega$. Such a resulted $-M_z$ state is very stable under the perturbation of $I_{ac} = 1 \mu$ A until another I_p is followed, demonstrating its non-volatile nature. Interestingly, I_p except the first one can only induce a sudden increase of R_{\perp}^{ω} from -1.2 to $0.2 \text{ k}\Omega$ during the application of I_p , the removal of which immediately drives R_{\perp}^{ω} back to $-1.2 \text{ k}\Omega$. Such a volatile switching can be well repeated by applying several subsequent I_p , in sharp contrast to the non-volatile one induced by the first I_p . This volatile switching is likely to originate in the DL-SOT demonstrated above because the lack of an in-plane field for a deterministic switching could cause the restoration to the initial magnetization after the disappearance of the I_p -induce SOT. However, there is no reason that the first I_p inducing the nonvolatile switching has a different effect when compared to the subsequent I_p that result in SOT-induced volatile switchings, except that the first I_p is applied to the special magnetic state that is preset by the magnetic history. To check this, we explore the I_p -magnitude dependence by varying from 20, 50, to 100 μ A respectively, and the result is shown in Fig. 3d. One can find the threshold $I_p \sim 50 \mu$ A, below which the change of R_{\perp}^{ω} by I_p is smaller than those above and in a step-by-step manner (as exemplified by the 20 μ A curve), which is nonvolatile. When above the threshold, the switching is accomplished right after applying the first I_p (as exemplified by the coincidence of the

50 and 100 μ A curves) while subsequent I_p cannot cause further change of R_{\perp}^{ω} . Thus, the amount of the switched magnetization rises with the I_p -magnitude before reaching the threshold, consistent with the DL-SOT origin. Such a threshold is much lower than those in metallic bilayers.

Phenomenological model. The above observed switching can be described by a phenomenological model in Fig. 3e. On the one hand, the perpendicular magnetic anisotropy of the CBST film is not strong enough to maintain a single domain at zero-field. So the magnetization shows a multidomain state at zero-field with the majority of domains preset by the applied magnetic field history (see Figs. 2c and 4c). This state may thus host some metastable states and be easy to be switched. On the other hand, since the ferromagnetism in CBST is induced by Cr dopants, which could not be ideally homogeneous, it results in an amount of magnetic grains isolated by different energy barriers. The formation of these magnetic grains, and thus their energy landscape, is a combined effect from the native crystalline topography, specific Cr-distribution, and the magnetic history. Whereas the former two cannot be changed for the as-grown thin film, the magnetic history that controls the magnetization energy of the grains then determines the switching process of these grains. The above two reasons lead to the energy landscape as shown in the left panel of Fig. 3e, which exhibits a native asymmetry preset by the magnetic history. Probably because of this, the nonvolatile switching would therefore only depend on the duration and magnitude of I instead of its polarity. The object of this non-volatile switching is likely to be the magnetic grains addressed above. ΔE in this picture could be determined by the grain

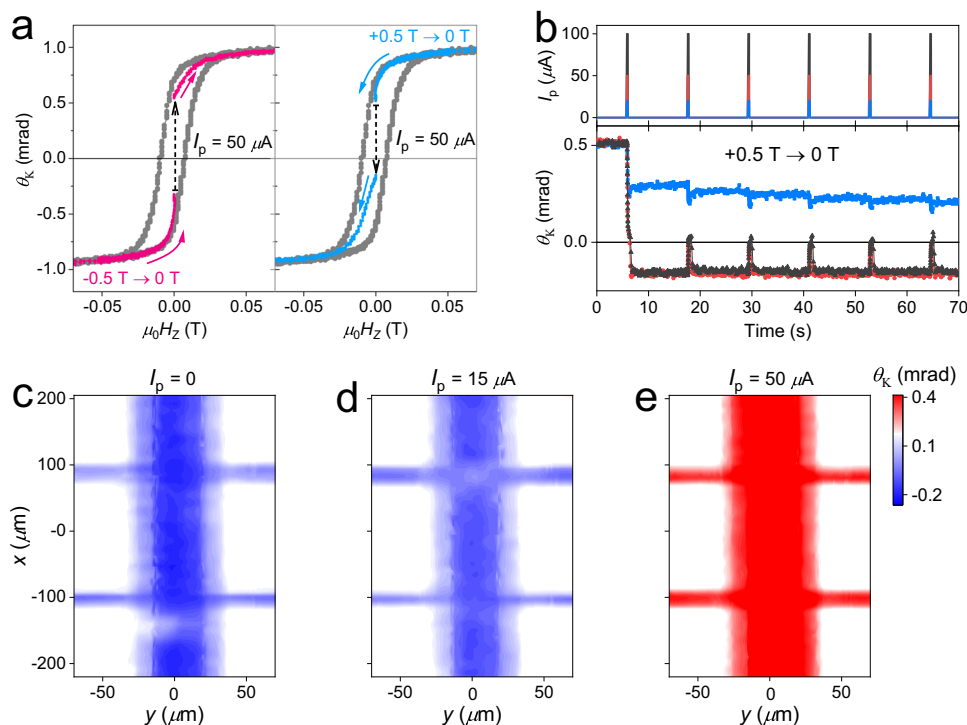


Fig. 4 Zero-field magnetization switchings probed by magneto-optical Kerr effect (MOKE). **a** $\mu_0 H_z$ -dependent Kerr rotation angle (θ_K). A pulse current I_p (50 μA , 200 ms) is applied under zero field, which results in a sudden change of θ_K (dashed arrow). The gray loops are the full hysteresis loops measured using I_{ac} as references. **b** θ_K when repeatedly applying I_p of different magnitudes under zero field. **c-e** After sweeping from -0.5T to 0 followed by applying I_p of different magnitudes, MOKE images are taken by spatially scanings around the Hall bar, confirming the zero-field magnetization switching. Due to the large the laser spot size ($\sim 15\ \mu\text{m}$), the MOKE signal varies gradually around edges. The mapping areas near edges exhibit color gradients when compared with those in the bulks, which have length scales of $\sim 12\text{--}14\ \mu\text{m}$, similar to the laser spot size. Due to this similar length scale and limited resolution, whether the switching process initiates from the edge remains unclear.

distribution (size, density, etc.), magnetic stiffness, magnetization, anisotropy, etc., which requires different activation energies (I_{dc} or I_p in this case) to drive the magnetic state out from various local minima. For the specific microscopic switching process, the magnetization switching in our single layer should be dominated by the domain wall propagation in the multidomain state under zero field. Furthermore, since our sample is in the micron-scale, the switching accomplished purely through a coherent rotation should be rather difficult. Usually, the switching process is initiated through a coherent rotation, i.e., the nucleation of a reversed domain via the applied torque/effective field. Then the domain wall propagates and further promotes the whole switching process. Such a process has also been observed through magnetic imaging⁵⁹. According to the experimental results, the final state looks more energetically stable than the initial state, as marked by the energy difference ΔE between them. Although the formation of this ΔE remains unclear but it should associate with the magnetic history based on the fact that the nonvolatile switching direction solely depends on the magnetization procedure, i.e., from $+M_z$ or $-M_z$ to zero field. After switching, the energy landscape is smoothed and the switched state becomes the only stable state. Therefore, the native asymmetry is removed. At this stage, the application of I_{dc} or I_p only results in metastable magnetic dynamics, the removal of which immediately restores the switched state.

Switching probed by MOKE. The nonvolatile and volatile switchings are further confirmed using MOKE measurements, which were performed simultaneously with transports. The nonvolatile switchings in Fig. 3a and Supplementary Fig. 6 are

reexamined by tracking the $\mu_0 H_z$ -dependent Kerr rotation angle (θ_K), and the results are shown in Fig. 4a and Supplementary Fig. 8, which show identical behaviors to those by transport. The transport results obtained using multiple- I_p of various magnitudes in Fig. 3d can also be reproduced by MOKE in Fig. 4b, in which the current threshold of the nonvolatile switching agrees with that in transport. The volatile switchings by subsequent multiple- I_p also recur consistently. The most direct evidence to the nonvolatile switching refers to the MOKE images which were obtained by spatially scanings around the Hall bar after demagnetizing from -0.5T to 0 followed by applying $I_p = 0, 15,$ and $50\ \mu\text{A}$, as shown in Fig. 4c–e respectively. The image without applying any I_p (Fig. 4c) can serve as a reference of the $-M_z$ state under zero field, which shows negative θ_K throughout the Hall bar. After $I_p = 15\ \mu\text{A}$ is applied, the magnitude of θ_K decreases but θ_K still stays negative, which indicates a partial switching of $-M_z$. With $I_p = 50\ \mu\text{A}$ above the threshold, θ_K throughout the Hall bar becomes positive, which signifies the $+M_z$ state resulted from magnetization switching. Such a process conforms with results in Fig. 4b using I_p smaller and greater than the threshold, strongly proving the nonvolatile zero-field switching by I_p .

Trivial effect in metallic system. To gain insights about the mechanism of the switching, similar experiments have been performed on a ferromagnet/heavy-metal multilayer Ta(3)/CoFeB(1.3)/MgO(1)/Ta(3) (unit: nm) with a perpendicular anisotropy. This multilayer can realize a conventional SOT-induced magnetization switching when applying an in-plane $\mu_0 H = 300\ \text{Oe}$ and a switching current $I_{dc} = \pm 10\ \text{mA}$. By applying different current combinations to the multilayer,

including $I_{ac} = 15 \mu\text{A} \sim 15 \text{ mA}$ and $I_{ac} (15 \mu\text{A}) + I_{dc} (100 \mu\text{A} \sim 15 \text{ mA})$, we found that I_{dc} functions no more than Joule heating when compared the results obtained by I_{ac} only (Supplementary Fig. 9), which is in contrast to those in the single-layer magnetic TI. This observation highlights the difference between the magnetic TI and the metallic multilayer in the present switching methodology. This difference may be ascribed to the difference in magnetic energy or anisotropy between the two systems.

Discussion

The presence of SOT generally requires the breaking of structural inversion symmetry. In the ferromagnet/heavy-metal bilayer this can be achieved by the native vertical asymmetry. In our single-layer system, the matrix material, $(\text{Bi,Sb})_2\text{Te}_3$, is a layered hexagonal material that has a trigonal axis (three-fold rotation symmetry), a binary axis (two-fold rotation symmetry), and a bisectrix axis (in the reflection plane)⁶⁰. Thus, there is no apparent symmetry breaking in terms of the crystalline structure. As the single layer exhibits nonreciprocal transport, like UMR above, there must be some inversion symmetry breaking in this system besides the time-reversal symmetry broken by the magnetic order. However, according to the intensity oscillation of a reflection high-energy electron diffraction (RHEED) during the epitaxial growth of the Cr-doped $(\text{Bi,Sb})_2\text{Te}_3$ layer (Supplementary Fig. 10), one can see that it takes $\sim 118 \text{ s}$ to grow the first layer, whereas it changes to $\sim 75 \text{ s}$ for each of the following layers. This originates in the lattice transition from the GaAs substrate (zinc-blende) to the Cr-doped $(\text{Bi,Sb})_2\text{Te}_3$ film (rhombohedral), during which the high-vapor-pressure materials Bi/Sb/Te are less prone to be deposited than the low-vapor-pressure metal Cr. This contrast may lead to a higher Cr-concentration in the first layer than those in the followings. Mathematically, the Cr-concentration in the first layer is $\sim 118 \text{ s}/75 \text{ s} = 1.57$ times of the following, but this number is overestimated since the Cr-deposition rate is not ideally constant but also depends on the Bi/Sb/Te-deposition rates. Therefore, the epitaxial process is likely to result in a compositional asymmetry in the Cr-profile, which may be the origin of the observed UMR and SOT. Another symmetry-breaking candidate may come from the structural inversion asymmetry between the top and bottom surfaces of the single layer due to the existence of the substrate, which is a well-known effect in magnetic TI thin film^{61–64}.

The above results have shown a large SOT extracted from the single-layer magnetic TI and volatile switchings induced by SOT, we thus intuitively regard that the SOT is likely to also play a role in nonvolatile switchings. When the Cr-concentration at the bottom surface of the single-layer magnetic TI is higher than that of the top, correspondingly, the gap opening at the bottom surface will be larger than that of the top. Due to the extremely small gap size (about the order of 10 meV) and the elevated temperature (like 4.5 K in the present study), surface electrons will be thermally excited to Fermi surface and contribute to transport. Because of the smaller gap on the top surface, more top surface electrons will be excited and contribute than those from the bottom, which will lead to a non-equilibrium spin accumulation. Since electrons from the top and bottom surfaces have helicities of opposite spin-momentum locking, this will lead to a non-zero SOT from the single layer. It could be plausible that the SOT kicks the initial magnetic state and induces the switching in assistance with the Joule heating.

The present study not only shows the existence of a large DL-SOT accompanied with UMR and nonlinear Hall effect in the single-layer magnetic TI but also provides a methodology to realize a zero-field magnetization switching using topological magnets and perspective on understanding SOT-induced

magnetization dynamics. This work can motivate research toward ultralow-power and scalable topological spintronic devices.

Methods

Film growth and device fabrication. The magnetic TI film used in this study is the modulation-doped Cr-doped $(\text{Bi,Sb})_2\text{Te}_3$ epitaxially grown on a semi-insulating GaAs (111)B substrate in a molecular beam epitaxy system. During the growth, the substrate was held at $\sim 200 \text{ }^\circ\text{C}$ with high purity Bi (6N) evaporated from a dual-filament cell, Cr (4N5) from a high-temperature cell, while Sb (6N) and Te (7N) from thermal cracker cells. Similar to refs. ^{65,66}, the top-one and bottom-one quintuple layer has a higher Cr concentration resulted from the Cr temperature of $1130 \text{ }^\circ\text{C}$, while the middle four quintuple layers have lower Cr concentration resulted from the Cr temperature of $1110 \text{ }^\circ\text{C}$, forming a magnetically-symmetric profile. The temperatures of remaining elements were fixed throughout the growth. The total thickness is six quintuple layers, corresponding to $\sim 6 \text{ nm}$, which was controlled by the reflection high-energy electron diffraction in situ. The films were patterned into Hall bars with $w = 50 \mu\text{m}$ and $l = 200 \mu\text{m}$ using standard photolithography and reactive ion etching. Contacts were made by depositing Ti (15 nm)/Au (85 nm) layers and bonded by Al wires.

Magneto-electrical transport. The Hall bar was loaded into a cryostat with the magnetic field created by a superconducting magnet. The current was applied by a Keithley 6221 current source meter and the voltage was picked up using lock-in amplifiers (SR830). The Hall bar can be rotated by a rotator on the cryogenic insert. The resulted Cr-doped $(\text{Bi,Sb})_2\text{Te}_3$ film is ferromagnetic with the Curie temperature of above 12 K as shown in Supplementary Fig. 11. In other transport measurements, the sample is held at 4.5 K so that all the currents in the present study can be applied without temperature increment higher than 0.2 K, while the signal-to-noise ratios of the measured quantities are still satisfactory.

MOKE measurement. The scanning magneto-optic Kerr effects measurement was carried out using an all-fiber zero-loop Sagnac interferometer similar to refs. ^{67,68} installed in a dilution refrigerator. A high sensitivity of $0.2 \mu\text{rad}$ is achieved with about $50 \mu\text{W}$ light incident onto the sample. A three-axis piezo scanner cooperating with a focusing gradient-index lens allows spatial mapping with resolution of $15 \mu\text{m}$. The probing light and applied magnetic field were perpendicular to the sample. The single-layer magnetic TI is much thinner than the skin depth of the operating wavelength of 1550 nm and the Kerr rotation angle induced by the intrinsic GaAs substrate is negligible. The detected Kerr rotation angle should be proportional to the out-of-plane magnetization⁶⁹.

Data availability

The data that support the findings of this study are available from the corresponding author upon reasonable request.

Received: 1 March 2023; Accepted: 14 August 2023;

Published online: 21 August 2023

References

- Manchon, A. et al. Current-induced spin-orbit torques in ferromagnetic and antiferromagnetic systems. *Rev. Mod. Phys.* **91**, 035004 (2019).
- Dyakonov, M. I. & Perel, V. I. Current-induced spin orientation of electrons in semiconductors. *Phys. Lett. A* **35**, 459–460 (1971).
- Hirsch, J. E. Spin Hall effect. *Phys. Rev. Lett.* **83**, 1834–1837 (1999).

4. Zhang, S. Spin Hall effect in the presence of spin diffusion. *Phys. Rev. Lett.* **85**, 393–396 (2000).
5. Edelstein, V. M. Spin polarization of conduction electrons induced by electric current in two-dimensional asymmetric electron systems. *Solid State Commun.* **73**, 233–235 (1990).
6. Dresselhaus, G. Spin-orbit coupling effects in zinc blende structures. *Phys. Rev.* **100**, 580–586 (1955).
7. Bychkov, Y. A. & Rashba, E. I. Properties of a 2d electron-gas with lifted spectral degeneracy. *JETP Lett.* **39**, 78–81 (1984).
8. Miao, B. F., Huang, S. Y., Qu, D. & Chien, C. L. Inverse spin Hall effect in a ferromagnetic metal. *Phys. Rev. Lett.* **111**, 066602 (2013).
9. Wu, S. M., Hoffman, J., Pearson, J. E. & Bhattacharya, A. Unambiguous separation of the inverse spin Hall and anomalous Nernst effects within a ferromagnetic metal using the spin Seebeck effect. *Appl. Phys. Lett.* **105**, 092409 (2014).
10. Seki, T. et al. Observation of inverse spin Hall effect in ferromagnetic FePt alloys using spin Seebeck effect. *Appl. Phys. Lett.* **107**, 092401 (2015).
11. Yagmur, A., Sumi, S., Awano, H. & Tanabe, K. Large inverse spin Hall effect in Co-Tb alloys due to spin Seebeck effect. *Phys. Rev. Appl.* **14**, 064025 (2020).
12. Tian, D. et al. Manipulation of pure spin current in ferromagnetic metals independent of magnetization. *Phys. Rev. B* **94**, 020403 (2016).
13. Das, K. S., Schoemaker, W. Y., van Wees, B. J. & Vera-Marun, I. J. Spin injection and detection via the anomalous spin Hall effect of a ferromagnetic metal. *Phys. Rev. B* **96**, 220408 (2017).
14. Iihama, S. et al. Spin-transfer torque induced by the spin anomalous Hall effect. *Nat. Electron.* **1**, 120–123 (2018).
15. Gibbons, J. D., MacNeill, D., Buhrman, R. A. & Ralph, D. C. Reorientable spin direction for spin current produced by the anomalous Hall effect. *Phys. Rev. Appl.* **9**, 064033 (2018).
16. Bose, A. et al. Observation of anomalous spin torque generated by a ferromagnet. *Phys. Rev. Appl.* **9**, 064026 (2018).
17. Seki, T., Iihama, S., Taniguchi, T. & Takanaishi, K. Large spin anomalous Hall effect in $L1_0$ -FePt: symmetry and magnetization switching. *Phys. Rev. B* **100**, 144427 (2019).
18. Omori, Y. et al. Relation between spin Hall effect and anomalous Hall effect in 3d ferromagnetic metals. *Phys. Rev. B* **99**, 014403 (2019).
19. Leiva, L. et al. Giant spin Hall angle in the Heusler alloy Weyl ferromagnet Co_2MnGa . *Phys. Rev. B* **103**, L041114 (2021).
20. Liu, L. et al. Electrical switching of perpendicular magnetization in a single ferromagnetic layer. *Phys. Rev. B* **101**, 220402 (2020).
21. Tang, M. et al. Bulk spin torque-driven perpendicular magnetization switching in $L1_0$ FePt single layer. *Adv. Mater.* **32**, 2002607 (2020).
22. Zhang, R. Q. et al. Current-induced magnetization switching in a CoTb amorphous single layer. *Phys. Rev. B* **101**, 214418 (2020).
23. Tang, K. et al. Magnetization switching induced by spin-orbit torque from Co_2MnGa magnetic Weyl semimetal thin films. *Appl. Phys. Lett.* **118**, 062402 (2021).
24. Xie, H. et al. Magnetization switching in polycrystalline Mn_3Sn thin film induced by self-generated spin-polarized current. *Nat. Commun.* **13**, 5744 (2022).
25. Liu, Q., Zhu, L., Zhang, X. S., Muller, D. A. & Ralph, D. C. Giant bulk spin-orbit torque and efficient electrical switching in single ferrimagnetic FeTb layers with strong perpendicular magnetic anisotropy. *Appl. Phys. Rev.* **9**, 021402 (2022).
26. Luo, Z. et al. Spin-orbit torque in a single ferromagnetic layer induced by surface spin rotation. *Phys. Rev. Appl.* **11**, 064021 (2019).
27. Zhu, L., Ralph, D. C. & Buhrman, R. A. Unveiling the mechanism of bulk spin-orbit torques within chemically disordered Fe_xPt_{1-x} single layers. *Adv. Funct. Mater.* **31**, 2103898 (2021).
28. Lee, J. W., Park, J. Y., Yuk, J. M. & Park, B.-G. Spin-orbit torque in a perpendicularly magnetized ferrimagnetic Tb-Co single layer. *Phys. Rev. Appl.* **13**, 044030 (2020).
29. Zheng, Z. et al. Field-free spin-orbit torque-induced switching of perpendicular magnetization in a ferrimagnetic layer with a vertical composition gradient. *Nat. Commun.* **12**, 4555 (2021).
30. Wang, W. et al. Anomalous spin-orbit torques in magnetic single-layer films. *Nat. Nanotechnol.* **14**, 819–824 (2019).
31. Seki, T., Lau, Y.-C., Iihama, S. & Takanaishi, K. Spin-orbit torque in a Ni-Fe single layer. *Phys. Rev. B* **104**, 094430 (2021).
32. Fu, Q. et al. Observation of nontrivial spin-orbit torque in single-layer ferromagnetic metals. *Phys. Rev. B* **105**, 224417 (2022).
33. Chen, Z. et al. Current-induced magnetization switching in a chemically disordered A1 CoPt single layer. *Appl. Phys. Express* **14**, 033002 (2021).
34. Xie, X. et al. Controllable field-free switching of perpendicular magnetization through bulk spin-orbit torque in symmetry-broken ferromagnetic films. *Nat. Commun.* **12** <https://doi.org/10.1038/s41467-41021-22819-4>, <https://doi.org/10.1038/s41467-021-22819-4> (2021).
35. Liu, L. et al. Current-induced self-switching of perpendicular magnetization in CoPt single layer. *Nat. Commun.* **13** <https://doi.org/10.1038/s41467-41022-31167-w>, <https://doi.org/10.1038/s41467-022-31167-w> (2022).
36. Huang, Q. et al. Field-free magnetization switching in a ferromagnetic single layer through multiple inversion asymmetry engineering. *ACS Nano* **16**, 12462–12470 (2022).
37. Krishnia, S. et al. Spin-orbit coupling in single-layer ferrimagnets: direct observation of spin-orbit torques and chiral spin textures. *Phys. Rev. Appl.* **16**, 024040 (2021).
38. Pai, C.-F. Switching by topological insulators. *Nat. Mater.* **17**, 755–757 (2018).
39. Fan, Y. et al. Magnetization switching through giant spin-orbit torque in a magnetically doped topological insulator heterostructure. *Nat. Mater.* **13**, 699–704 (2014).
40. Fan, Y. B. et al. Electric-field control of spin-orbit torque in a magnetically doped topological insulator. *Nat. Nanotechnol.* **11**, 352–359 (2016).
41. Han, J. et al. Room-temperature spin-orbit torque switching induced by a topological insulator. *Phys. Rev. Lett.* **119**, 077702 (2017).
42. Wang, Y. et al. Room temperature magnetization switching in topological insulator-ferromagnet heterostructures by spin-orbit torques. *Nat. Commun.* **8**, 1364 (2017).
43. Khang, N. H. D., Ueda, Y. & Hai, P. N. A conductive topological insulator with large spin Hall effect for ultralow power spin-orbit torque switching. *Nat. Mater.* **17**, 808–813 (2018).
44. Dc, M. et al. Room-temperature high spin-orbit torque due to quantum confinement in sputtered $Bi_xSe_{(1-x)}$ films. *Nat. Mater.* **17**, 800–807 (2018).
45. Li, P. et al. Magnetization switching using topological surface states. *Sci. Adv.* **5**, eaaw3415 (2019).
46. Chen, L. et al. Connections between spin-orbit torques and unidirectional magnetoresistance in ferromagnetic-metal-heavy-metal heterostructures. *Phys. Rev. B* **105**, L020406 (2022).
47. Miron, I. M. et al. Perpendicular switching of a single ferromagnetic layer induced by in-plane current injection. *Nature* **476**, 189–193 (2011).
48. Liu, L. et al. Spin-torque switching with the giant spin Hall effect of tantalum. *Science* **336**, 555–558 (2012).
49. Liu, L., Lee, O. J., Gudmundsen, T. J., Ralph, D. C. & Buhrman, R. A. Current-induced switching of perpendicularly magnetized magnetic layers using spin torque from the spin Hall effect. *Phys. Rev. Lett.* **109**, 096602 (2012).
50. Yasuda, K. et al. Large unidirectional magnetoresistance in a magnetic topological insulator. *Phys. Rev. Lett.* **117**, 127202 (2016).
51. Avci, C. O., Mendil, J., Beach, G. S. D. & Gambardella, P. Origins of the unidirectional spin Hall magnetoresistance in metallic bilayers. *Phys. Rev. Lett.* **121**, 087207 (2018).
52. Fan, Y. et al. Unidirectional magneto-resistance in modulation-doped magnetic topological insulators. *Nano Lett.* **19**, 692–698 (2019).
53. Avci, C. O. et al. Unidirectional spin Hall magnetoresistance in ferromagnet/normal metal bilayers. *Nat. Phys.* **11**, 570–575 (2015).
54. Avci, C. O. et al. Magnetoresistance of heavy and light metal/ferromagnet bilayers. *Appl. Phys. Lett.* **107**, 192405 (2015).
55. Vaz, D. C. et al. Determining the Rashba parameter from the bilinear magnetoresistance response in a two-dimensional electron gas. *Phys. Rev. Mater.* **4**, 071001 (2020).
56. Dyrdał, A., Barnaś, J. & Fert, A. Spin-momentum-locking inhomogeneities as a source of bilinear magnetoresistance in topological insulators. *Phys. Rev. Lett.* **124**, 046802 (2020).
57. He, P. et al. Bilinear magnetoelectric resistance as a probe of three-dimensional spin texture in topological surface states. *Nat. Phys.* **14**, 495–499 (2018).
58. He, P. et al. Nonlinear planar Hall effect. *Phys. Rev. Lett.* **123**, 016801 (2019).
59. Baumgartner, M. et al. Spatially and time-resolved magnetization dynamics driven by spin-orbit torques. *Nat. Nanotechnol.* **12**, 980–986 (2017).
60. Zhang, H. et al. Topological insulators in Bi_2Se_3 , Bi_2Te_3 and Sb_2Te_3 with a single Dirac cone on the surface. *Nat. Phys.* **5**, 438–442 (2009).
61. Zhang, S.-F., Jiang, H., Xie, X. C. & Sun, Q.-F. Effect of magnetic field on a magnetic topological insulator film with structural inversion asymmetry. *Phys. Rev. B* **89**, 155419 (2014).
62. Wang, J., Lian, B. & Zhang, S.-C. Electrically tunable magnetism in magnetic topological insulators. *Phys. Rev. Lett.* **115**, 036805 (2015).
63. Lu, H.-Z., Zhao, A. & Shen, S.-Q. Quantum transport in magnetic topological insulator thin films. *Phys. Rev. Lett.* **111**, 146802 (2013).
64. Wang, J., Lian, B. & Zhang, S.-C. Quantum anomalous Hall effect in magnetic topological insulators. *Phys. Scr.* **T164**, 014003 (2015).
65. Mogi, M. et al. Magnetic modulation doping in topological insulators toward higher-temperature quantum anomalous Hall effect. *Appl. Phys. Lett.* **107**, 182401 (2015).
66. Pan, L. et al. Probing the low-temperature limit of the quantum anomalous Hall effect. *Sci. Adv.* **6**, eaaz3595 (2020).

67. Xia, J., Beyersdorf, P. T., Fejer, M. M. & Kapitulnik, A. Modified Sagnac interferometer for high-sensitivity magneto-optic measurements at cryogenic temperatures. *Appl. Phys. Lett.* **89**, 062508 (2006).
68. Fried, A., Fejer, M. & Kapitulnik, A. A scanning, all-fiber Sagnac interferometer for high resolution magneto-optic measurements at 820 nm. *Rev. Sci. Instrum.* **85**, 103707 (2014).
69. Qiu, Z. Q. & Bader, S. D. Surface magneto-optic Kerr effect (SMOKE). *J. Magn. Magn. Mater.* **200**, 664–678 (1999).

Acknowledgements

This work is supported in part by the National Key R&D Program of China (Grant Nos. 2020YFA0308900, 2018YFA0305601), the National Natural Science Foundation of China (Grant No. 11874070), and the Strategic Priority Research Program of Chinese Academy of Sciences (Grant No. XDB28000000).

Author contributions

Q.L.H. and H.S. conceived the research. H.S. and Y.H. grew the magnetic TI films. H.S. performed experiments on material characterizations, device fabrications, and all the transport measurements. D.H., H.S., and Yang L. performed the MOKE measurements and related data analysis. X.L. and G.Y. grew the metallic multilayer and fabricated devices. W.S. performed the magnetization measurements. Yizhou L., H.S., and Q.L.H. performed data analyses and fittings. The paper was written by Q.L.H. with contributions from H.S., Yizhou L., D.H., Y.F., Y.H., M.H., X.L., W.S., Yang L., and G.Y.

Competing interests

The authors declare no competing interests.

Additional information

Supplementary information The online version contains supplementary material available at <https://doi.org/10.1038/s42005-023-01349-z>.

Correspondence and requests for materials should be addressed to Qing Lin He.

Peer review information *Communications Physics* thanks Gyung-Min Choi and the other, anonymous, reviewer(s) for their contribution to the peer review of this work.

Reprints and permission information is available at <http://www.nature.com/reprints>

Publisher's note Springer Nature remains neutral with regard to jurisdictional claims in published maps and institutional affiliations.



Open Access This article is licensed under a Creative Commons Attribution 4.0 International License, which permits use, sharing, adaptation, distribution and reproduction in any medium or format, as long as you give appropriate credit to the original author(s) and the source, provide a link to the Creative Commons licence, and indicate if changes were made. The images or other third party material in this article are included in the article's Creative Commons licence, unless indicated otherwise in a credit line to the material. If material is not included in the article's Creative Commons licence and your intended use is not permitted by statutory regulation or exceeds the permitted use, you will need to obtain permission directly from the copyright holder. To view a copy of this licence, visit <http://creativecommons.org/licenses/by/4.0/>.

© The Author(s) 2023